INTERNATIONAL JOURNAL FOR NUMERICAL METHODS IN FLUIDS
*Int. J. Numer. Meth. Fluids* 2006; **51**:1–29
Published online 15 November 2005 in Wiley InterScience (www.interscience.wiley.com). DOI: 10.1002/fld.1094

# Numerical simulation of incompressible viscous flow past a heaving airfoil

Sunetra Sarkar[‡] and Kartik Venkatraman[*,†]

*Department of Aerospace Engineering, Indian Institute of Science, Bangalore 560012, India*

SUMMARY

Numerical simulations of a heaving airfoil undergoing non-sinusoidal motions in an incompressible viscous flow is presented. In particular, asymmetric sinusoidal motions, constant heave rate oscillations, and sinusoidal motions with a quiescent gap, are considered. The wake patterns, thrust force coefficients, and propulsive efficiency at various values of non-dimensional heave velocity are computed. These have been compared with those of corresponding sinusoidal heaving motions of the airfoil. It is shown that for a given non-dimensional heave velocity and reduced frequency of oscillation, asymmetric sinusoidal motions give better thrust and propulsive efficiencies in comparison to pure harmonic motion. On the other hand, constant rate heave motion do not compare favourably with harmonic motion. A train of sinusoidal pulses separated by a quiescent gap compares favourably with a pure sinusoidal motion, but with the notable exception that the quiescent gap induces a discontinuity that induces large impulses to the wake pattern. Copyright © 2005 John Wiley & Sons, Ltd.

KEY WORDS: oscillating airfoil; unsteady aerodynamics; discrete vortex method

## 1. INTRODUCTION

The ability of a plunging airfoil to generate thrust is well known. This phenomenon is known as the Knoller–Betz or Katzmayer effect. Many researchers have performed experimental and numerical studies on purely plunging and flapping airfoil and on their thrust generation characteristics and wake patterns. A thrust generating foil shows a wake pattern behind its trailing edge which is opposite in sense to a Karman vortex street. The flow past a plunging airfoil is of interest not only in understanding the fluid dynamics of birds, insects, and aquatic animal propulsion, but also useful in designing flapping foil micro-air vehicles [1].

Heaving airfoil motions have been studied for quite sometime now. Garrick [2] has shown using linearized potential flow theory that for small amplitude heaving oscillation, thrust force

*Correspondence to: Kartik Venkatraman, Department of Aerospace Engineering, Indian Institute of Science, Bangalore 560012, India.
†E-mail: kartik@aero.iisc.ernet.in
‡E-mail: sunetra@aero.iisc.ernet.in

*Received 22 November 2004*
*Revised 1 July 2005*
*Accepted 2 July 2005*

exists at all frequencies. Lighthill [3], has also theoretically calculated the thrust force and efficiency for an inviscid and nonlinear flow model. This study also predicts positive thrust at every frequency, and shows that propulsion efficiency is maximum as the frequency approaches zero. Jones *et al.* [4], have performed water tunnel experiments for flow visualization of the unsteady wake behind plunging airfoils. Numerical simulations with an inviscid unsteady panel code is also presented. The non-dimensional plunge velocity, $k\bar{h}$, is shown to be an important parameter for thrust generation and the nature of the wake vortex patterns. $\bar{h}$ is the heave amplitude normalized by the airfoil chord $c$, and $k$ is the reduced frequency $k = \omega c/V_\infty$. At high values of $k\bar{h}$, wake deflection was also observed. Tuncer and Platzer [5] used a compressible Navier–Stokes solver at a low subsonic Mach number to study the unsteady flow patterns and thrust characteristics of a plunging and a combination of plunging and pitching motion. Triantafyllou *et al.* [6] show that the reduced frequency or Strouhal number is an important parameter to study thrust generation characteristics. Lai and Platzer [7] conducted water-tunnel experiments on a plunging airfoil and conclude that airfoil motion having non-dimensional plunge velocity below $k\bar{h} = 0.43$ produce drag, while those above produce thrust. A thrust producing wake pattern become asymmetric and deflected from their mean position at values of $k\bar{h} > 1$. Lewin and Haj-Hariri [8] have numerically studied viscous flow past a two-dimensional sinusoidally heaving airfoil over a range of frequencies and amplitudes. Vortex patterns and thrust characteristics, as well as propulsive efficiencies have been computed. They have found asymmetric and deflected vortex patterns as the Strouhal number increases. At a given Strouhal number, the maximum efficiency occurs at an intermediate frequency, not in the low-frequency range as suggested by inviscid theories. It is presumed that at low frequencies, significant leading edge vortex shedding results in loss of thrust. On the other hand, in the high-frequency region, efficiency decreases with increase in frequency, in agreement with the prediction of ideal fluid theory. Wang [9] has also observed this phenomenon. The Reynolds numbers for these studies were in the range of 500–1000. Isogai *et al.* [10] have studied the compressible viscous flow past an airfoil in combined pitch and heave motion with phase difference between them. The influence of phase angles and reduced frequencies, as well as two different pitch to heave amplitude ratios, on the propulsive efficiency have been examined. Anderson *et al.* [11] have experimentally studied the propulsive performance of a harmonically oscillating airfoil in both heave and pitch and have observed optimum parameter ranges. Results have also been compared with linear and nonlinear inviscid theories. Read *et al.* [12] define an equivalent angle of attack for combined heave and pitch motion of an airfoil. At high Strouhal numbers, the angle of attack $\alpha$ shows multiple peaks in one period. A higher-order harmonic motion in heave can achieve significant thrust recovery in such cases. Hover *et al.* [13] have extended a similar study with various non-sinusoidal angle of attack $\alpha$ profiles and compared their propulsive performance. Koochesfahani [14] has made some interesting experimental observations with a pitching airfoil undergoing asymmetric sinusoidal oscillations.

The present work is a numerical study of viscous incompressible flow past an airfoil heaving in a near-sinusoidal oscillatory motion. Three such motions are considered. One is the asymmetric sinusoid which is a sinusoid excepting that the downstroke is faster/slower than the upstroke. The asymmetry parameter $S$ defines the fraction of the time-period it takes to complete the upstroke. The second type of motion considered is the constant heave rate in the upstroke and downstroke. This results in a triangular waveform. The third and final type of motion studied is the sinusoidal pulse train. The vorticity patterns of the flow for such

 

motions, as well as thrust generated and propulsive efficiency, are computed and compared with purely sinusoidal heaving motion.

## 2. THE RANDOM DISCRETE VORTEX METHOD

An incompressible viscous flow can be described in terms of its vorticity $\mathbf{\Omega} = \nabla \times \mathbf{V}$ as [15]

$$\frac{\mathrm{D}\mathbf{\Omega}}{\mathrm{D}t} = \partial\mathbf{\Omega}/\partial t + \mathbf{V}.\nabla\mathbf{\Omega} = \mathbf{\Omega}.\nabla\mathbf{V} + v\nabla^2\mathbf{\Omega} \tag{1}$$

where $v$ is the viscosity and $\mathbf{V}$ is the velocity field. The $\mathbf{\Omega}.\nabla\mathbf{V}$ term gives the rate of deformation of the vortex lines and exists only in three-dimensional flow. Hence for a 2-D incompressible flow the vorticity transport equation is rewritten in the form

$$\frac{\mathrm{D}\Omega}{\mathrm{D}t} = v\nabla^2\Omega \tag{2}$$

The relationship between the vorticity and the stream function is given by the Poisson equation

$$\nabla^2\psi = -\Omega \tag{3}$$

where $\psi$ is the stream function. In this representation, the far-field boundary condition that the flow remains undisturbed needs to be carefully dealt with during numerical implementation [16].

The relationship between the vorticity and the velocity field is given by a vector Poisson equation [15, 17]

$$\nabla^2\mathbf{V} = -\nabla \times \mathbf{\Omega} \tag{4}$$

The solution to this vector Poisson equation with appropriate boundary condition uniquely defines the velocity–vorticity relationship, and is expressed as an integral representation that is similar to the Bio–Savart law of electromagnetic theory [15, 17, 18]. Now the velocity field is determined from the known vorticity distribution in the fluid region $R$, as well as the velocity boundary conditions on the surface S of the solid body as well as the far-field. This integral relation is given by [17]

$$\mathbf{V}(\mathbf{r}, t) = -\frac{1}{2\pi}\left[\int_R \frac{\mathbf{\Omega} \times (\mathbf{r}_0 - \mathbf{r})}{|\mathbf{r}_0 - \mathbf{r}|^2}\,\mathrm{d}R + 2\int_S \frac{\mathbf{\Omega}_b \times (\mathbf{r}_0 - \mathbf{r})}{|\mathbf{r}_0 - \mathbf{r}|^2}\mathrm{dS} + \mathbf{V}_\infty\right] \tag{5}$$

where $\mathbf{\Omega}_b$ is the rigid body angular velocity of the solid whose boundary is denoted by S, and $\mathbf{V}_\infty$ its translational velocity (Figure 1). $\mathbf{r}_0$ is the vector distance from the origin of the reference frame to the vortex particles in the fluid region $R$, and $\mathbf{r}$ is the point in the flow-field where the induced velocity due to these vortex particles are to be determined. Note that the velocity field automatically satisfies the far-field velocity boundary condition of the flow being undisturbed.

The discrete vortex numerical simulation that we have used in this study of heaving airfoil motion will use the vorticity evolution Equation (2) together with the relation for the velocity field in terms of the vorticity given by Equation (5).

 

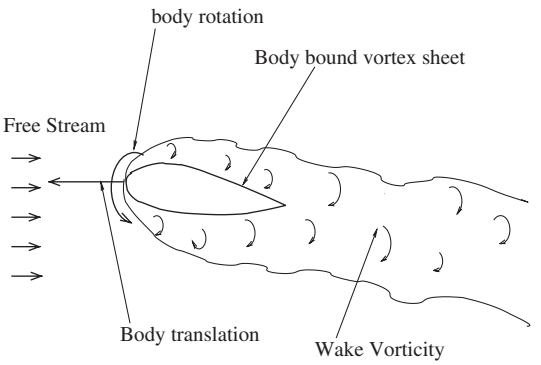


Figure 1. Schematic diagram of a translating and rotating body in the flow field.

Equation (2) can be split into convection and diffusion parts and can be solved sequentially. This is known as operator splitting [19]. Thus, Equation (2) can be represented as

$$\partial\Omega/\partial t + \mathbf{V}.\nabla\Omega = 0 \tag{6}$$

$$\partial\Omega/\partial t = v\nabla^2\Omega \tag{7}$$

Equation (6) represents the convection of the vorticity in the fluid region. The convective velocity component induced by the vortex particles in the fluid region $R$ is given by the Biot–Savart relation Equation (5). Equation (7) represents the diffusion of the vorticity. The solution of the diffusion equation (7) is identical to the probability density function of a Gaussian random variable with a zero mean and standard deviation $\sqrt{2t/Re}$ [15]. Therefore, in the discrete vortex technique of modelling viscous incompressible flow, the diffusion of the vorticity is modelled as a random walk [19]. Diffusion then is simulated as a displacement of the vortex element in the two orthogonal directions using two independent sets of Gaussian random numbers. These Gaussian random numbers will have zero mean and a variance of $2\Delta t/Re$, where $\Delta t$ is the time interval [20]. This technique gives good convergence for the Navier–Stokes equation, if the number of discrete vortices used in the formulation is sufficiently large.

In summary, the convective displacement of the vortex particle, for each time step, is determined from the convective velocity component. The displacement due to the diffusion component, after each time step, is determined from the random walk simulation. The total displacement of any discrete vortex particle, after each time step, then will be the sum of the displacements due to convection and diffusion.

The vorticity is generated at the fluid–solid boundary interface. This is done by enforcing the no-slip and no-penetration boundary conditions on the body surface S. The near-field boundary condition at the body surface states that the fluid velocity at any point on the body surface $\mathbf{V}(\mathrm{S})$ is equal to the velocity of the body $\mathbf{V}_b$ at that point

$$\mathbf{V}(\mathrm{S}) = \mathbf{V}_b \tag{8}$$

To enforce the near-field boundary conditions, a body bound vortex sheet is assumed. The solution of this unknown vortex sheet is obtained by assuming the no-normal flow condition

 

on the body surface

$$(\mathbf{V} - \mathbf{V}_b).\hat{n} = 0 \tag{9}$$

where $\hat{n}$ denotes the normal vector to the body boundary. This body bound vortex sheet, in general, will not satisfy the no-slip condition. Therefore, the non-zero tangential velocity is nullified by generating free vortices at the surface. The vorticity flux of this free vorticity in the normal direction to the body surface is given by [21–23]

$$\nu \frac{\partial \Omega}{\partial \hat{n}}(s) = -\gamma(s)/\delta t \tag{10}$$

where the left-hand side is the local vorticity flux, $\gamma(s)$ is the vortex sheet strength as a function of path length $s$ along the boundary, and $\delta t$ is the time interval. The vorticity flux is assumed to be constant over time interval $\delta t$.

### 2.1. Numerical implementation

The two-dimensional body surface is divided into a number of straight line panels with the collocation points at the centre. A vortex node is designated at each panel mid-point. A body bound vortex sheet is assumed over the body surface, where the strength of the vortex sheet at each panel is an unknown. The no-normal flow boundary condition, so as to compute the strength of this unknown vortex sheet, is satisfied at the mid-point of each panel. However, in order to keep the continuity of the vortex sheet strength across the panels, a linearly varying vortex strength is assumed [24]. At the end of each time step, the vortices corrected for the no-slip flow boundary condition are created at a distance $\delta$ above the body surface. In this procedure, we further sub-divide each panel into a number of sub-panels, and one vortex per sub-panel is released into the flow. A thin fictitious region close to the body surface is assumed and is referred to as the control zone with a thickness $\Delta$ [18]. This is shown schematically in Figure 2. The creation of new vortices takes place inside this control zone. The newly created vortices are actually within the boundary of this so-called control zone, when they are released from the surface satisfying no-slip. However, the control zone may already have a number of vortices present as a left-over from the previous time step. This could happen when some of the newly created vortices, after convection and diffusion at the previous time step, might fail to cross the control zone boundary and stay inside. Therefore, at the next time step when again newly created vortices join them, they are combined with the newly created vortices of respective panels to give the resultant nascent vortices. The process of nascent vortex creation has been depicted in Figure 3. It needs careful selection of the thickness of the control zone as it affects the simulation. The thickness of the control zone is finalized after a trial and error procedure and the same has been used for all the calculations.

The no-normal flow boundary condition at each panel mid-point, in order to compute the panel vorticity strength is represented as

$$\mathbf{V}_{\mathrm{fs},i} + \mathbf{V}_{\mathrm{vf},i} + \mathbf{V}_{\mathrm{vc},i} + \mathbf{V}_{\mathrm{bm},i} = 0 \tag{11}$$

Equation (11) states that the sum of the normal velocities induced at panel mid-point $i$ due to the free stream ($\mathbf{V}_{\mathrm{fs},i}$), vortices outside the control zone ($\mathbf{V}_{\mathrm{vf},i}$), vortices inside the control

 

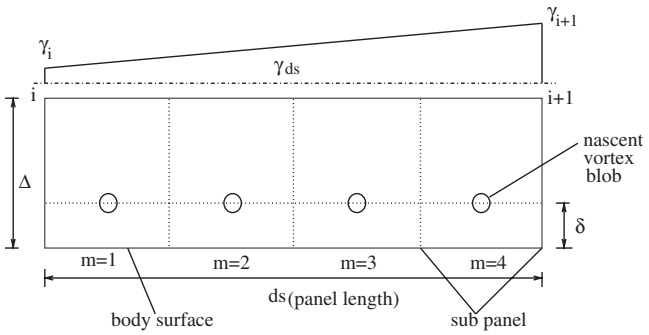


Figure 2. Schematic diagram depicting control zone and nascent vortex blobs.

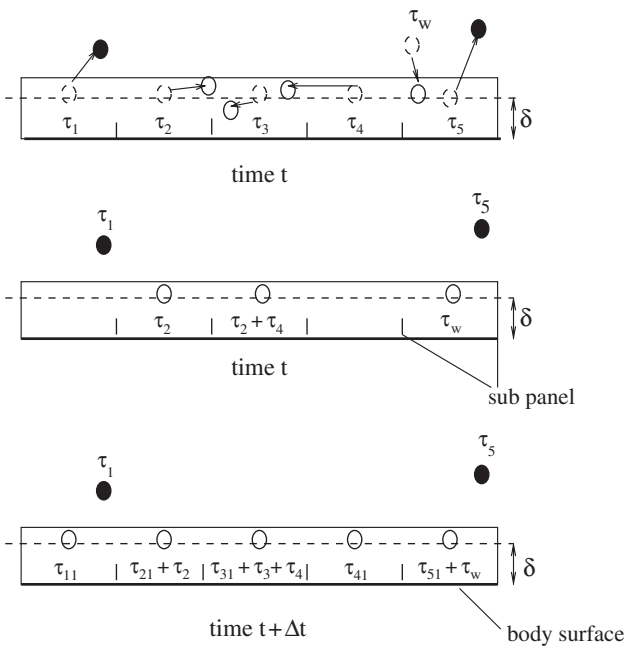


Figure 3. Vortex movement in and out of the control zone and nascent vortex creation at each time step.

zone ($\mathbf{V}_{\mathrm{vc},i}$), and by the body motion ($\mathbf{V}_{\mathrm{bm},i}$) is equal to zero. There will be as many number of equations as the number of unknown panel vortex strengths. However, as there are no source/sink terms in the flow model, one equation in this set will be redundant. Therefore an additional condition is needed to obtain unique panel vorticity strengths. This additional condition is obtained from the principle of conservation of circulation or what is known as

 

Kelvin's theorem [18]

$$\sum \Gamma_v + \sum_{j=1}^{j=N} \Gamma_j + \Gamma_{\text{bm}} = \Gamma_{\text{st}} \tag{12}$$

where the first term $\sum \Gamma_v$ represents the summation of the circulation of the wake vortices, the second term denotes the circulation of the unknown nascent vortices inside the control zone for a total of $N$ number of panels, $\Gamma_{\text{bm}}$ is the circulation due to body motion, and $\Gamma_{\text{st}}$ is the circulation in the flow field prior to the start of simulation. Figure 1 shows the schematic diagram of a body with generalized motion in the flow field. The vortices created at the body boundary go out of the control zone following convection and diffusion. If the vortex sheet strength of any panel at time $t$ be $\gamma_1$, and the panel vortex sheet strength remaining within the control zone from the previous time step $(t - \Delta t)$, after convection and diffusion, be $\gamma_2$, then from Equation (10)

$$(\gamma_1 - \gamma_2) = -\nu \frac{\partial \Omega}{\partial n} \Delta t \tag{13}$$

Each surface panel is further sub-divided into a number of sub-panels, and after the creation of the vortices at each panel, they are broken down into vortex blobs at each of the sub-panels [18]. These blobs are later convected and diffused. Each blob is assumed to have symmetrical vorticity distribution defined by a stream function [19]

$$\psi(r) = \begin{cases} \dfrac{\log(\mathbf{r})}{2\pi} & (\mathbf{r} \geqslant \sigma) \\ \dfrac{\mathbf{r}/\sigma}{2\pi} & (\mathbf{r} < \sigma) \end{cases} \tag{14}$$

where $\sigma$ is the cut-off radius. This ensures that outside the $\sigma$ range, vortices follow the Bio–Savart law of velocity, and inside the $\sigma$ range, the velocity is constant.

The study uses 160 panels with 5 subpanels in each of them. This makes a total of 800 vortices generated at any time step. The airfoil chord length $c = 1$, $\sigma = 0.0022$, and $\Delta = 0.0088$. These values were finalized after some trial and error, and validation of results with the available literature. An important entity which can control the accuracy of the numerical scheme is the time interval. As we have already seen in Equation (10), the time step size should be small enough to ensure that the vorticity flux generated from the body can be assumed to be constant over the interval. We have followed a first-order time marching scheme for the simulations, and it gives reasonably good results with a sufficiently small time step size of $\Delta t = 0.005$ s.

The forces exerted on the body arise from two major sources, namely the surface pressure and surface friction. The tangential pressure gradient on the body surface is given by

$$\frac{1}{\rho} \frac{\partial p}{\partial \hat{s}} = -\hat{s}.\frac{\mathrm{D}\mathbf{V}_b}{\mathrm{D}t} - \hat{n}.\mathbf{r}\frac{\mathrm{D}\Omega_b}{\mathrm{D}t} + \hat{s}.\mathbf{r}\Omega_b^2 + \nu \frac{\partial \Omega}{\partial \hat{n}} \tag{15}$$

where $\rho$ is the constant density of the fluid, $\mathbf{V}_b$ is the translational velocity of the body motion and $\Omega_b$ is the angular velocity of the body motion. $\hat{s}$ and $\hat{n}$ denote the unit vectors in the

 

body tangential and normal directions. The last term on the right-hand side of the equation can be evaluated by using Equation (13). The shear stress or friction ($\tau$) on a solid boundary in a Newtonian fluid is given by

$$\tau = \mu \frac{\partial u_s}{\partial \hat{n}} \tag{16}$$

Here, $u_s$ is the velocity component tangential to the surface. Equations (15) and (16) can be integrated to calculate the aerodynamic loads from the surface pressure distribution.

The mean propulsive efficiency $\eta$ is defined as the ratio of the mean thrust force generated times the free-stream airspeed $\mathbf{V}_\infty$ and the average input work done. The input work done is calculated by taking force normal to the horizontal flow times the local heave velocity [5, 9].

## 3. KINEMATICS

Sinusoidal oscillations are probably the most common form of periodic oscillation found in real life biological locomotion. However, we are interested to compare the sinusoidal cases with various non-sinusoidal motions in terms of thrust generation and propulsive efficiency. Various types of complex non-sinusoidal motions are realizable in man-made small scale thrust generating devices like MAVs or robotic biological locomotion simulators like robo-fishes, etc. Our interest is to see if such motions can actually improve the capabilities of these devices.

Sinusoidal plunging or heaving motion about an axis parallel to the streamwise velocity is given by

$$\begin{aligned} h_o(t) &= h \sin(\omega t) \\ v_o(t) &= h\omega \cos(\omega t) \end{aligned} \tag{17}$$

where $h$ is the amplitude in plunge, and $\omega$ is the frequency of oscillation. If we rescale time as $\tau = \mathbf{V}_\infty t/c$, non-dimensionalize the heave displacement amplitude as $\bar{h} = h/c$, define the heave velocity $v_o(\tau) = \mathrm{d}h_o(\tau)/\mathrm{d}\tau$ and $k = \omega c/\mathbf{V}_\infty$. Then the non-dimensional displacement and velocity are given by

$$\begin{aligned} \bar{h}_o(\tau) &= \bar{h} \sin(k\tau) \\ \bar{v}_o(\tau) &= \bar{h}k \cos(k\tau) \end{aligned} \tag{18}$$

Previous studies indicate that the non-dimensional heave velocity amplitude $\bar{h}k$ is an important parameter to study the thrust generation and nature of wake vortex pattern [4, 7].

We compare the performance of sinusoidally heaving airfoil with many non-sinusoidal cases. In this category, we first consider an asymmetric sinusoidal heaving motion. The asymmetry is defined by a parameter $S$ that is defined as the fraction or percentage of the time-period of one cycle required to reach the maximum amplitude starting from the minimum amplitude. Following this definition, $S = 50\%$ implies a perfect sinusoidal waveform. One can represent

 

this type of waveform mathematically as

$$h_o(t) = h\sin\left(\frac{2\pi}{2ST}t - \pi/2\right), \quad 0 \leqslant t \leqslant ST$$
$$h_o(t) = h\sin\left(\frac{2\pi}{2(1-S)T}t + \pi/2\right), \quad ST \leqslant t \leqslant T \tag{19}$$

In the above $T$ is the time-period of the motion. Some examples of these type of motions are shown in Figure 7.

Another type of non-sinusoid waveform chosen for analysis here is a constant rate heaving oscillations with the upstroke and downstroke rates same, as shown in Figure 17. An equivalent sinusoidal waveform is also superposed there.

$$h_o(t) = \frac{4h}{T}t$$
$$v_o = \frac{4h}{T} \tag{20}$$

If we define the non-dimensional heave rate as $v_o(t)/\mathbf{V}_\infty$, then its relation with the non-dimensional heave rate for a sinusoidal oscillation having the same time-period is given by

$$\frac{v_o}{\mathbf{V}_\infty} = \frac{2}{\pi}\bar{h}k \tag{21}$$

Finally, we also consider a heave motion that comprises a sine variation with a gap for a fraction of the time-period, as shown in Figure 22(a).

All the above cases have been simulated in real time $t$ with a time interval discussed in the earlier section. The chord length and the free stream velocity have both been assumed to be unity for all the calculations.

## 4. DISCUSSION

The focus of the present study is to observe the qualitative wake patterns behind a plunging airfoil as well as to calculate the thrust force, and propulsive efficiency. The frequency of oscillation parameter $k$ is varied in a medium to high frequency range. Sinusoidal heave motion of the airfoil is first analysed. Subsequently, we consider the heave motions that are not sinusoidal during the oscillating cycle. We assume that the airfoil is at zero degree angle of attack; that is, the stroke plane is normal to the horizontal plane. However, for small values of angle of attack, the aerodynamic loads can be obtained by rotating the loads obtained for the zero degree angle of attack case by the appropriate angle. But for very high angle of attack, where huge separation and dynamic stall phenomena are likely to occur, this transformation may not be applicable.

### *4.1. Sinusoidal motion*

As discussed earlier in Section 1, the non-dimensional heave velocity $k\bar{h}$ plays an important role in the wake vortex behaviour and the thrust generation characteristics. Note that

 

$k\bar{h} = (\omega h_o/\mathbf{V}_\infty)$ is the non-dimensional heave velocity amplitude. In the present study we consider three different values of $k\bar{h}$—0.5, 1.0, and 1.5. For each of these values of the heave velocity, the reduced frequency is varied between the values 3 and 8. The Reynolds number of the flow is fixed at $1 \times 10^4$. The vortex patterns at these $k\bar{h}$ values are all thrust producing and therefore they are opposite in sense to a drag producing Karman vortex street.

Figure 4 shows the wake vortex patterns and the drag coefficient history at $k\bar{h} = 0.5$ for three different values of the reduced frequency. At the lower frequency values, the wake

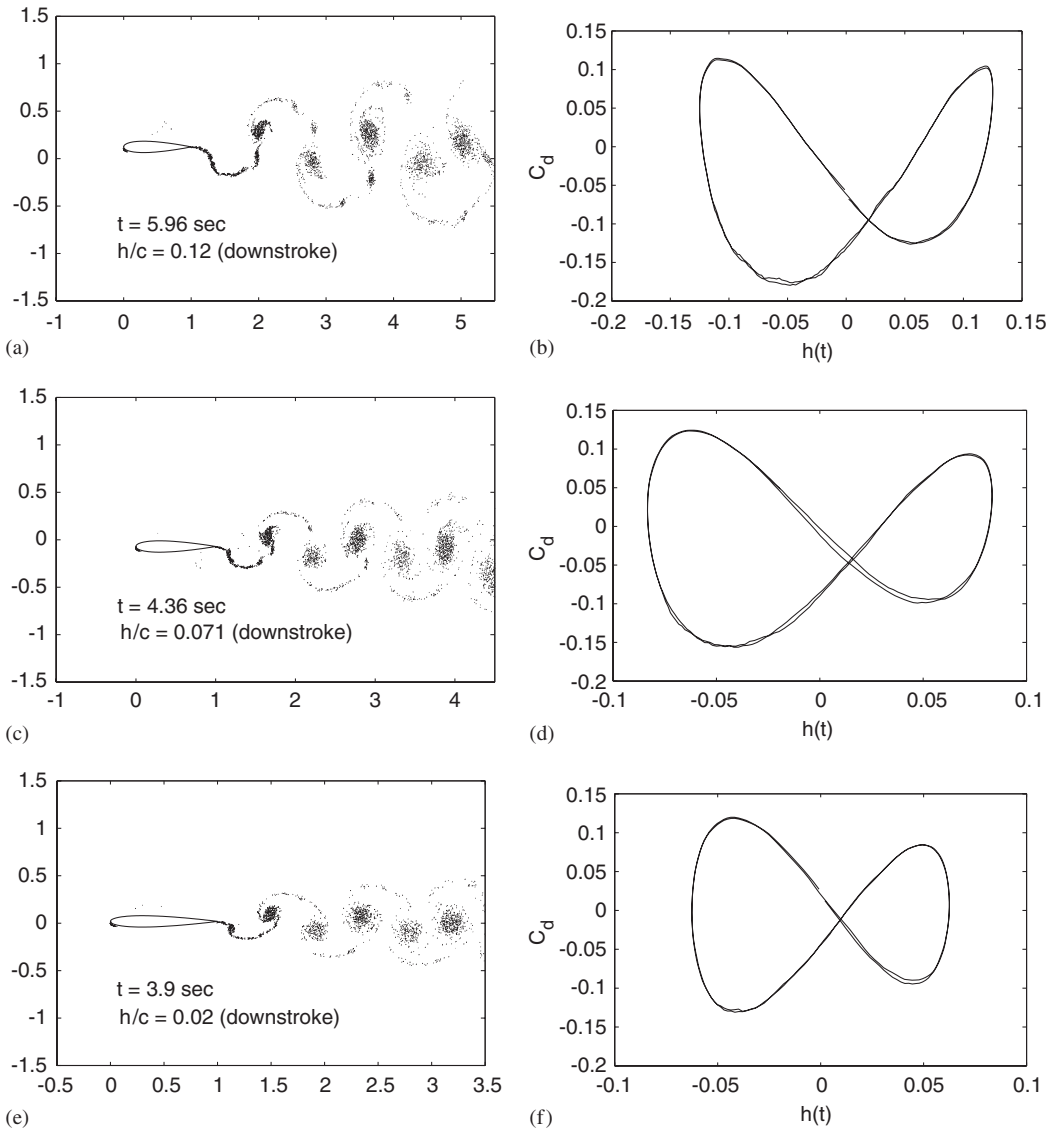


Figure 4. Unsteady wake patterns and drag history for sinusoidally heaving airfoil at different reduced frequencies, $k\bar{h} = 0.5$: (a) and (b) $k = 4$; (c) and (d) $k = 6$; and (e) and (f) $k = 8$.

 

vortex pattern does not seem to be as smooth as that at the higher frequencies. Traces of weak leading edge vortices in between strong trailing edge vortices can be identified from the wake pattern at $k = 4$, as seen in Figure 4(a). At higher frequencies however, the wake behind the trailing edge look more smooth. This is because at higher frequencies, the leading edge vortices are gradually dissipated into the trailing edge wake rather than being shed and convected. Also, at $k\bar{h} = 0.5$, the wake patterns are seen to be more or less symmetric with reference to the upstroke and downstroke of the heave motion.

When $k\bar{h} = 1.0$, a slight deflection of the wake pattern was observed. This deflection is more prominent at the higher reduced frequencies.

Figure 5 shows the vortex patterns and drag coefficients for $k\bar{h} = 1.5$. In this case, the wakes are clearly deflected from their mean positions. We did not observe any switching of the deflected wake during the cycles of heave oscillation that were simulated. Jones *et al.* [4] have observed mode switching in their water tunnel experiments. They argue that mode switching is triggered by very small perturbations. They did not observe any mode switching in their numerical simulations using an inviscid model. Lewin and Haj-Hariri [8] have presented mode switching for a similar value of $k\bar{h}$ and at $k = 8$ and 10. However, they have not discussed the exact number of oscillation cycles after which the switching occurs.

Figure 6 presents the average thrust coefficient ($C_T$) and the average propulsive efficiency ($\eta$) values as a function of $k$ for all the above cases. Thrust is defined as negative of the drag force. The thrust coefficient is almost constant with varying $k$ at a given value of non-dimensional velocity $k\bar{h}$. Further, for a given reduced frequency value, the thrust coefficient increases with increasing $k\bar{h}$ values. Given the limited data set of $k\bar{h}$ values, one might hazard a guess that this increase is nonlinear. The propulsive efficiency $\eta$ increases when $k\bar{h}$ increases from 0.5 to 1.0. Thereafter there is a decrease. Only at $k\bar{h} = 0.5$ is there a pronounced drop in efficiency as the reduced frequency increases. The linear potential flow theory of Garrick [2] predicts that propulsive efficiency should decrease with increasing reduced frequency. In the present study, in the higher frequency range, the same trend is observed. Moreover, in the present study, we have not observed any major leading edge separation, unlike some earlier studies carried out at much lower values of Reynolds numbers [8, 9]. At lower Reynolds number, the stronger viscous effects help grow and stabilize the leading edge vorticity.

### *4.2. Asymmetric sinusoidal motion*

An asymmetry parameter $S\%$ is defined as the fraction or percentage of the time-period of one cycle required to reach the maximum amplitude starting from the minimum amplitude. $S = 50\%$ implies the waveform is a perfect sinusoid. For example, $S$ lower than 50% implies a faster rate during the downstroke half of the heave cycle than the upstroke half. Example waveforms have been shown in Figure 7 for $S = 30, 50$, and 60%. We discuss the results for $S = 30$ and 60%.

*4.2.1. $kh = 0.5$.* Figure 8 shows the wake patterns and drag histories at three different reduced frequency values with $k\bar{h} = 0.5$ and asymmetry parameter set at $S = 30\%$. For this value of $S$ the downstroke of the cycle is executed faster than the upstroke. There is significant qualitative difference in the wake pattern compared to the pure sinusoidal case shown in Figure 4. Multiple vortices of the same sign are formed during the slower upstroke half of the heave cycle, whereas, one strong vortex is formed during the faster part. The wake patterns at all

 

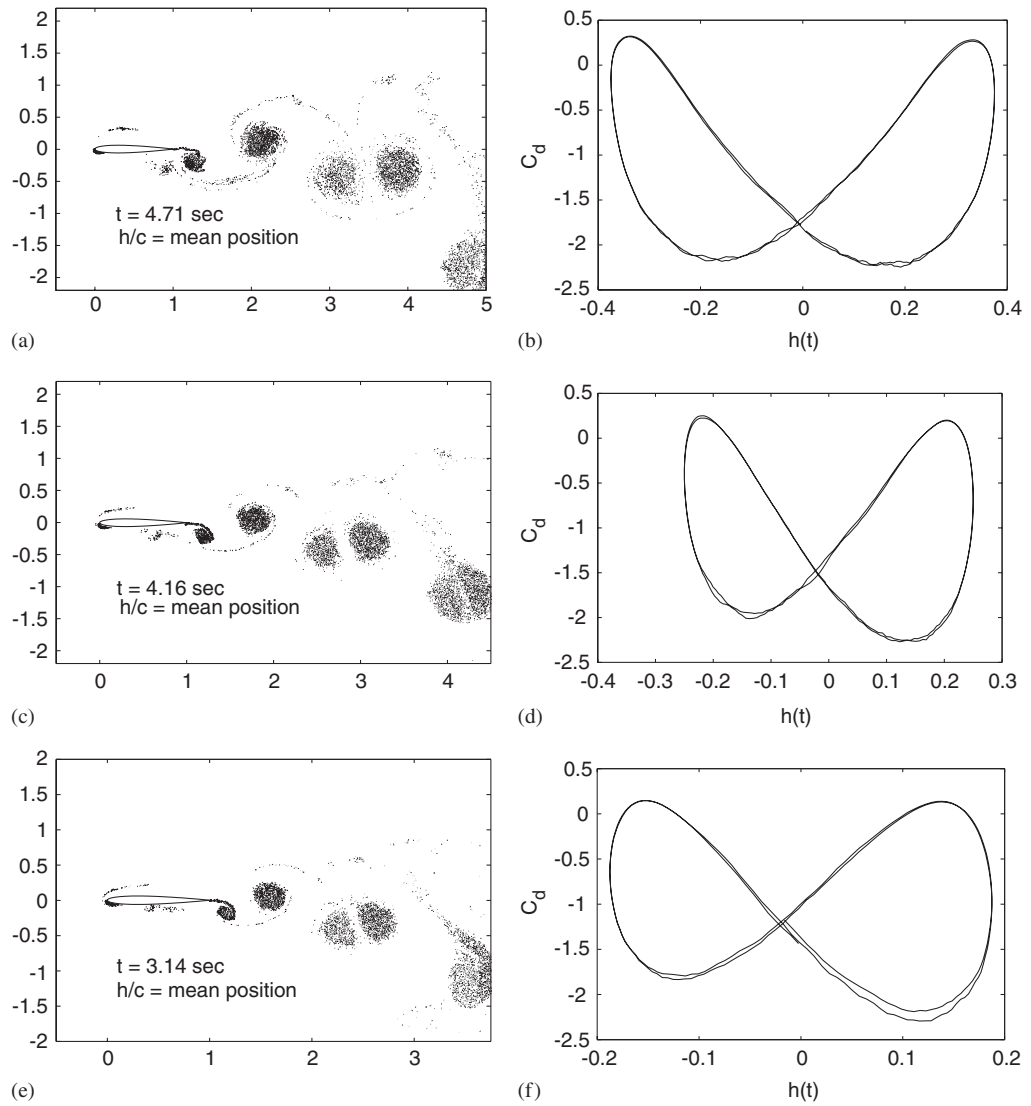


Figure 5. Unsteady wake patterns and drag history for sinusoidally heaving airfoil at different reduced frequencies, $k\bar{h} = 1.5$: (a) and (b) $k = 4$; (c) and (d) $k = 6$; and (e) and (f) $k = 8$.

the frequency values show a slight upward deflection. The shape of the wake and the vortex pairing also changes from cycle to cycle. At higher values of the reduced frequency the vortices are more diffused.

When $S = 60\%$, for $k\bar{h} = 0.5$, Figure 9 shows the wake vortex patterns and the drag coefficients at various reduced frequencies. Note that for this value of $S$ the downstroke is slower than the upstroke. The wake deflection is now downward. More than one same signed vortices are shed during the slower downstroke half of the cycle.

 

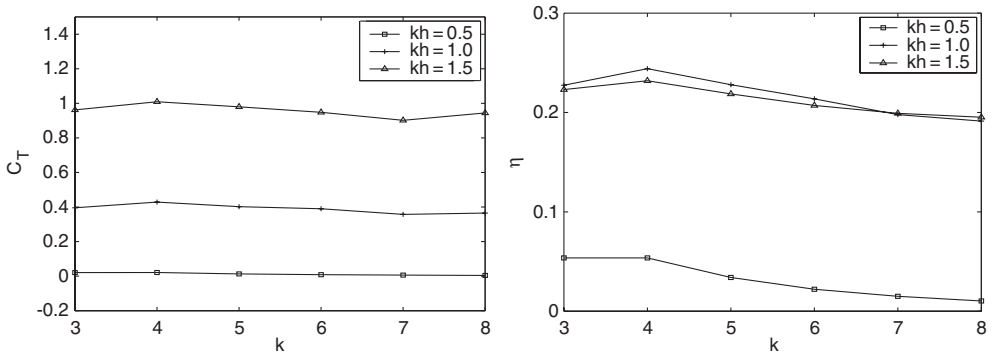


Figure 6. Average thrust coefficient and propulsive efficiency at different reduced frequencies.

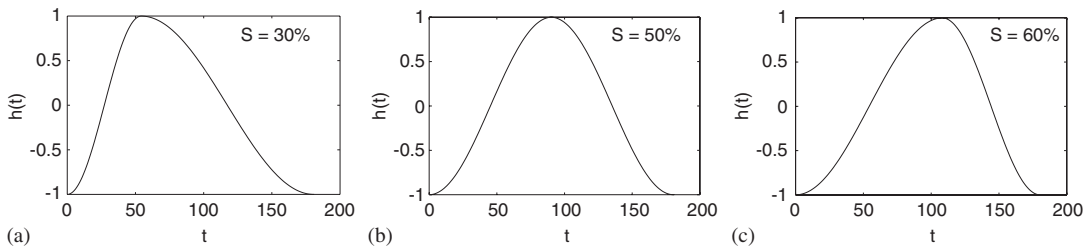


Figure 7. Asymmetric sinusoidal waveform as defined by the symmetry parameter $S$: (a) $S = 30\%$; (b) $S = 50\%$ (pure sine); and (c) $S = 60\%$.

Consider now the drag variation with heave displacement. Note that in Figure 8, for the fast downstroke, the drag value starts from a near-zero value at the top of the stroke and ends in a near-zero value near the bottom. Large amount of thrust force is generated during this half cycle. However, during the returning slow upstroke, the force pattern does not show much variation and smaller level of thrust force is generated. In contrast, for $S = 60\%$, as shown in Figure 9, the drag variation is anti-symmetric to the one shown for $S = 30\%$. There is very little variation in the slow downstroke, and very large variation in the fast upstroke.

*4.2.2. $kh = 1.0$.* The wake pattern shows again multiple vortices of the same sign which are formed during the slower half of the heave cycle. The vortex pairing pattern gets modified from cycle to cycle. For $S < 50\%$ the wake vortices are deflected upward, and for $S > 50\%$ downward. The magnitude of the deflection is more than that for the case $k\bar{h} = 0.5$. It was further observed that for this case of $k\bar{h}$, the wake vorticity looks more diffused than the earlier case.

*4.2.3. $kh = 1.5$.* Similar patterns are also observed for $k\bar{h} = 1.5$ too, as shown in Figures 10 and 11. The trailing wake is displaced upward relative to the free stream for $S < 50\%$, and displaced downward for $S > 50\%$. The displacement magnitude increases further than in the

 

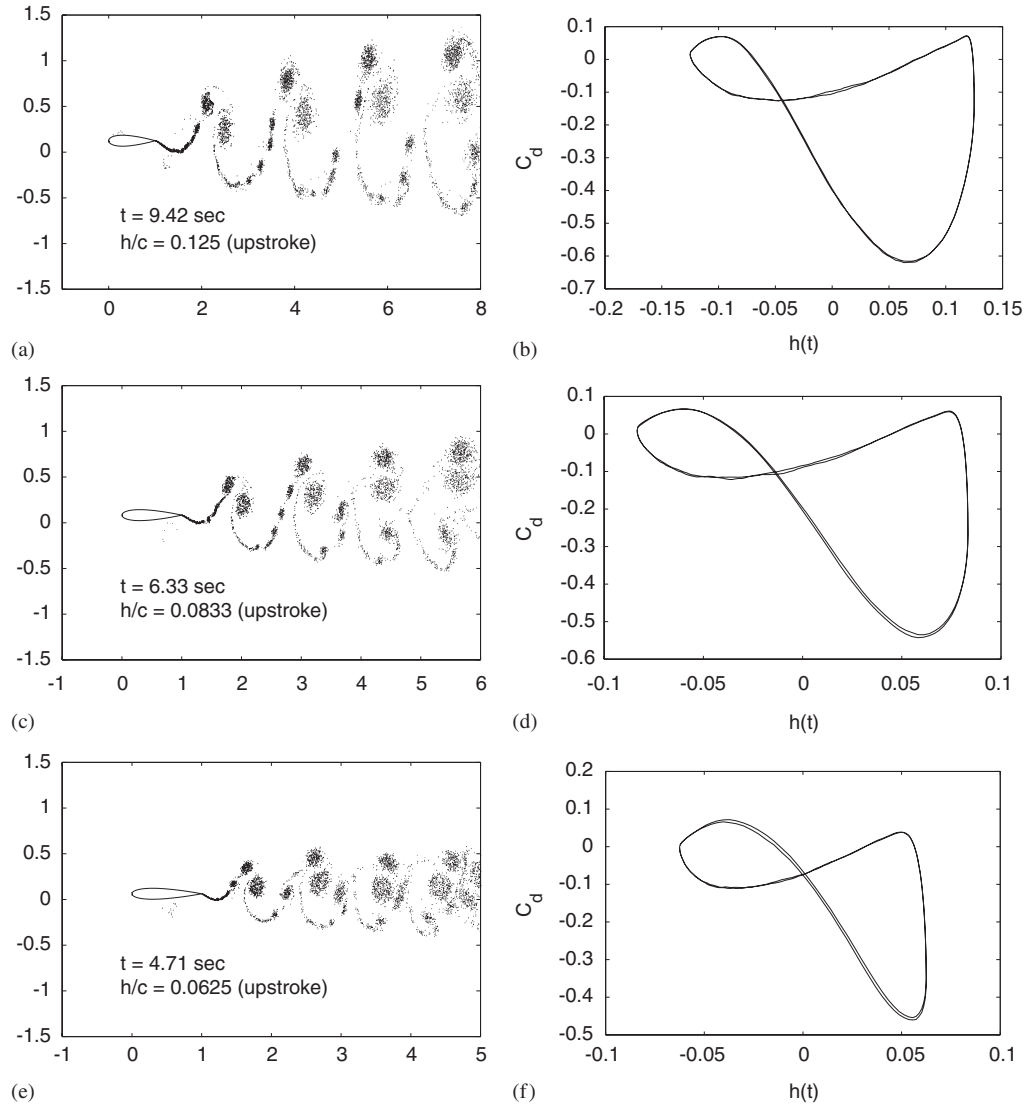


Figure 8. Unsteady wake patterns and drag history at different reduced frequencies, $k\bar{h} = 0.5$, $S = 30\%$: (a) and (b) $k = 4$; (c) and (d) $k = 6$; and (e) and (f) $k = 8$.

case of $k\bar{h} = 1.0$. Further, the wake vortex appears much more diffused. The tendency of the wake to appear diffused increases with increase in reduced frequency.

The thrust force and the propulsive efficiency for all these cases have been compared with their corresponding sinusoidal cases. In Figure 12, the thrust coefficient and propulsive efficiency for different values of $kh$ have been compared. For a given $k\bar{h}$ value, the thrust force is always minimum for the pure sinusoidal case compared to the asymmetric cases. The

 

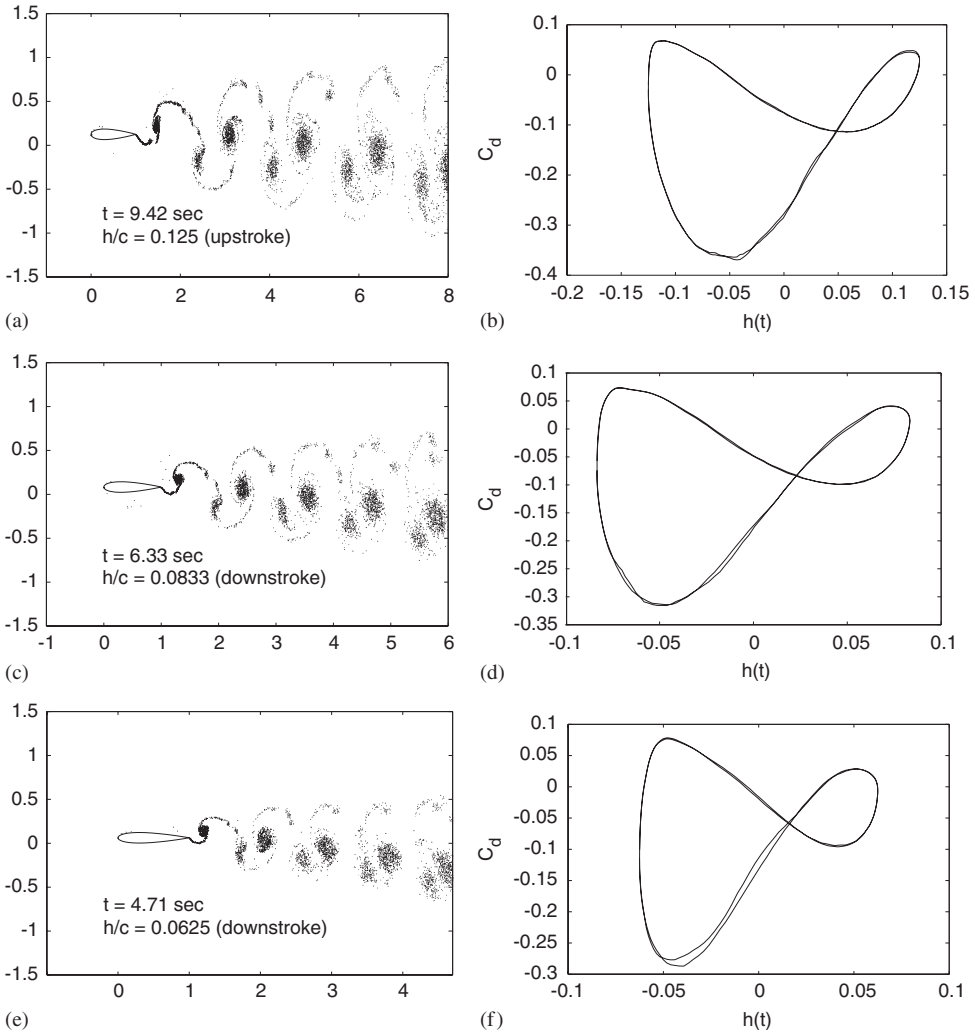


Figure 9. Unsteady wake patterns and drag history at different reduced frequencies, $k\bar{h} = 0.5$, $S = 60\%$: (a) and (b) $k = 4$; (c) and (d) $k = 6$; and (e) and (f) $k = 8$.

more the asymmetry, or in other words the faster the motion reaches one extrema from the other, the more the thrust generated. Further, the thrust coefficient reduces with frequency for all values of the non-dimensional heave velocity amplitude. For a given reduced frequency, the thrust coefficient increase with heave velocity amplitude, for any given value of $S$.

The propulsive efficiency trends though are not clear. For $k\bar{h} = 0.5$ the propulsive efficiency is greater if the rise or fall of amplitude is faster. But at $k\bar{h} = 1.0$ this is not true. The propulsive efficiency seems to be the same for all values of $S$, except in the lower and upper reduced frequency range of the bandwidth considered. However, the propulsive efficiency decreases with increase in $k$.

 

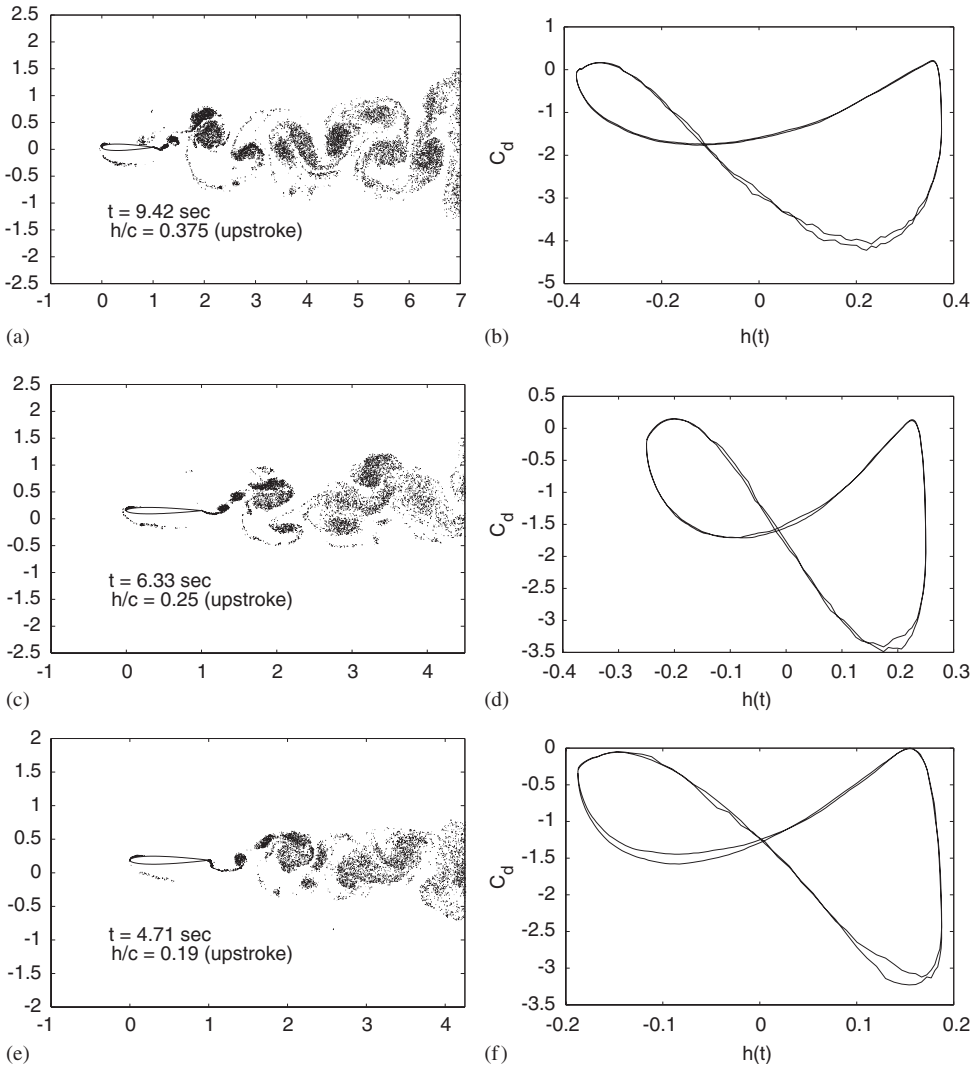


Figure 10. Unsteady wake patterns and drag history at different reduced frequencies, $k\bar{h} = 1.5$, $S = 30\%$: (a) and (b) $k = 4$; (c) and (d) $k = 6$; and (e) and (f) $k = 8$.

Though not shown here, the lift coefficient variation with $k$ for different values of the asymmetry parameter follows the same trend as in the case of the thrust coefficient. That is, the lift force generated is more when the sinusoidal motion is more asymmetric. This is true for the three different values of $k\bar{h}$ values that we simulated.

We have also shown the wake pattern for different values of $S$. Figures 13 and 14 shows the vortex pattern for $k = 7$ and $k\bar{h} = 0.5$ as the symmetry parameter of the non-sinusoidal motion changes from 20 to 80%. There is an upward deflection of the wake for $S < 50\%$, and a downward deflection for $S > 50\%$. It is clear that, as the asymmetry factor goes towards

 

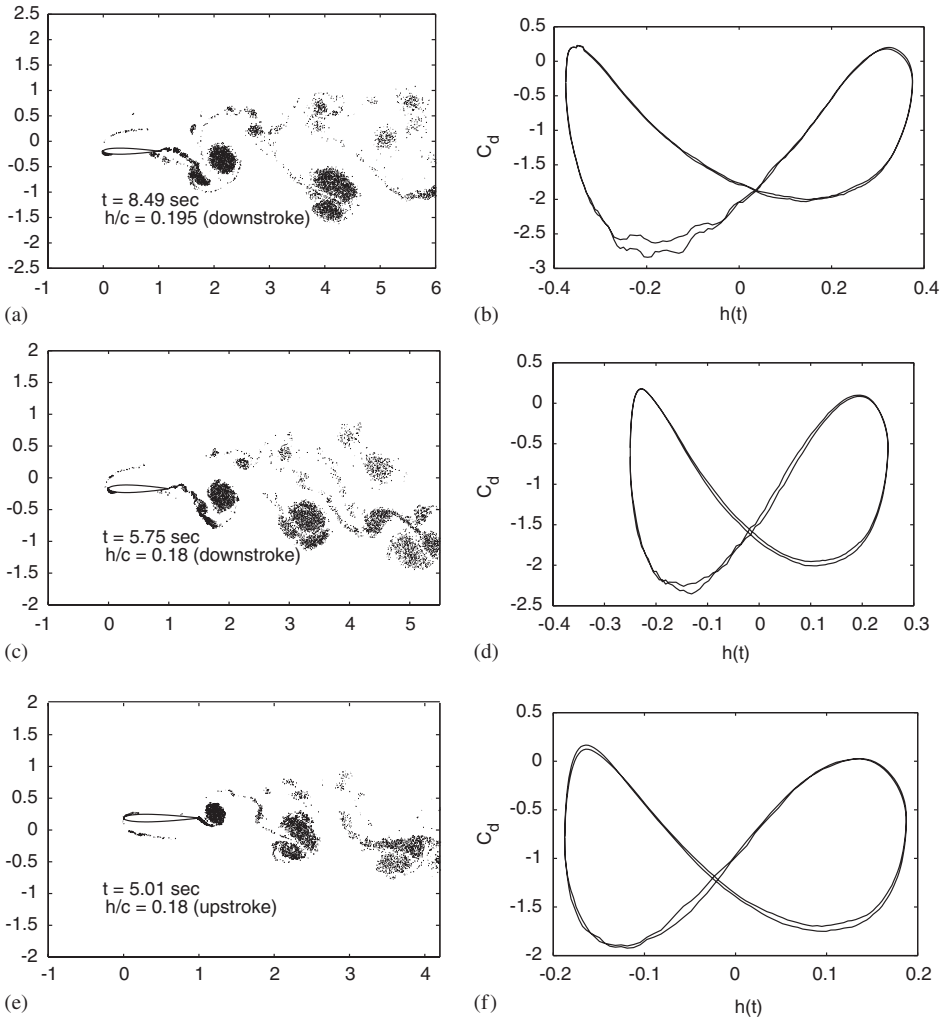


Figure 11. Unsteady wake patterns and drag history at different reduced frequencies, $k\bar{h} = 1.5$, $S = 60\%$: (a) and (b) $k = 4$; (c) and (d) $k = 6$; and (e) and (f) $k = 8$.

the perfect sinusoidal value, that is towards $S = 50\%$, the deflection from the mean position decreases, that is the upstroke and the downstroke becomes more similar. The change in shape in the wake vortex pairing is also more prominent with the increase in the asymmetry.

The average aerodynamic thrust and the propulsive efficiency at various values of $S$ have been calculated for $k\bar{h} = 0.5$ and 1.0, for $k = 7$. For both values of $k\bar{h}$, thrust coefficient $C_T$ shows a minimum at $S = 50\%$. The propulsive efficiency at $k\bar{h} = 0.5$, also follows the same trend. However, for $k\bar{h} = 1.0$, minimum efficiency is observed for $S = 20$ and 80%, that is, when the asymmetry factors are maximum. This is shown in Figure 15.

In summary, then, for maximum propulsive efficiency and thrust, values of $k\bar{h}$ greater than one is preferable, $S$ should be away from 50% or in other words the asymmetry should be

 

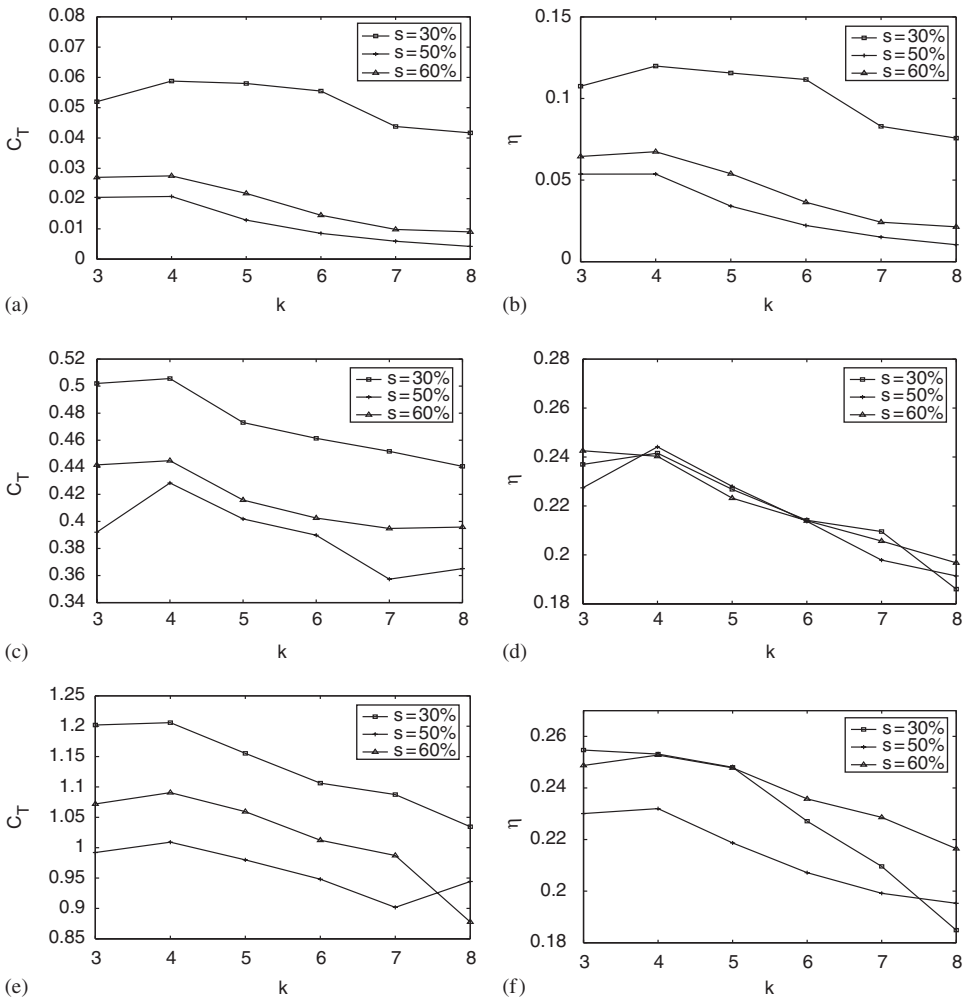


Figure 12. Variation of thrust coefficient and propulsive efficiency with reduced frequency: (a) and (b) $k\bar{h} = 0.5$; (c) and (d) $k\bar{h} = 1.0$; and (e) and (f) $k\bar{h} = 1.5$.

more. Note that when $S < 50\%$, the downstroke is relatively faster executed than the upstroke. Higher the rate, more the vorticity generated by the airfoil during its oscillation cycle.

Jones *et. al.* [4] have discussed about the switching of wake deflection mode (that is upwards or downwards) by changing the initial condition. However, in their experimental studies, they have observed mode switching to happen randomly on its own. This was not observed in their numerical simulations using an inviscid model. In the present study too, we have not observed any mode switching to occur on its own. However, we have been able to see mode switching after altering the initial conditions. A typical case with $k = 6$ and $k\bar{h} = 0.5$ have been presented in Figure 16. For $S = 30\%$, shown in Figures 16(a) and (b), a downward

 

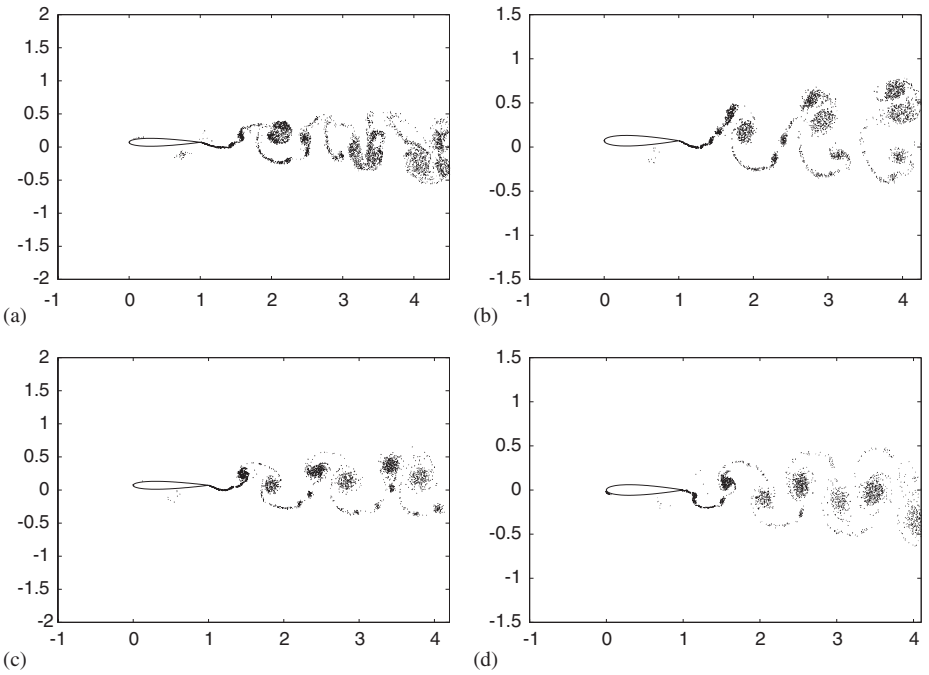


Figure 13. Unsteady wake patterns with different shape functions, $k\bar{h} = 0.5$, $k = 7$: (a) $S = 20\%$; (b) $S = 30\%$; (c) $S = 40\%$; and (d) $S = 50\%$. Instantaneous $h/c = 0.07$ (upstroke) for all asymmetric sinusoidal case, for $S = 50\%$, airfoil is at the mean position downwards.

deflection is observed now, after considering an opposite initial condition. In the earlier case the wake deflection was upward. For $S = 60\%$, with an opposite initial condition, we get an upward deflected wake, unlike the earlier observation.

### *4.3. Constant heave-rate motion*

We have also simulated a few cases of constant rate heaving motions. A typical motion time-history is shown in Figure 17 along with an equivalent sinusoidal motion. In this study, we consider different constant rates of heaving. The non-dimensional heaving rate is defined by $v_o/\mathbf{V}_\infty$. Each rate is compared with its equivalent sinusoidal reduced frequency $k$. The relation between the non-dimensional constant heave rate and $k$ is $v_o/\mathbf{V}_\infty = 2/\pi k\bar{h}$. $\bar{h}$ in this case also refers to the heave amplitude normalized with respect to the chord length. We set $\bar{h} = 0.2$ in all the simulations for this type of motion. The non-dimensional heave rate values considered in this study are namely $0.4, 0.6, 0.8$, and $1.0$. These then correspond to values of $k$ equal to $\pi$, $3\pi/2$, $2\pi$, and $5\pi/2$, respectively.

The wake patterns and the variation of the drag coefficient are plotted in Figures 18 and 19 for the values of heave rate considered. The effect of increasing the non-dimensional heave rate is very similar to that of increasing the reduced frequency for the sinusoidal case. At lower rates, as shown in Figure 18, there are traces of shed leading edge vortices between two strong trailing edge vortices. Further, note that there is wake deflection at higher rates.

 

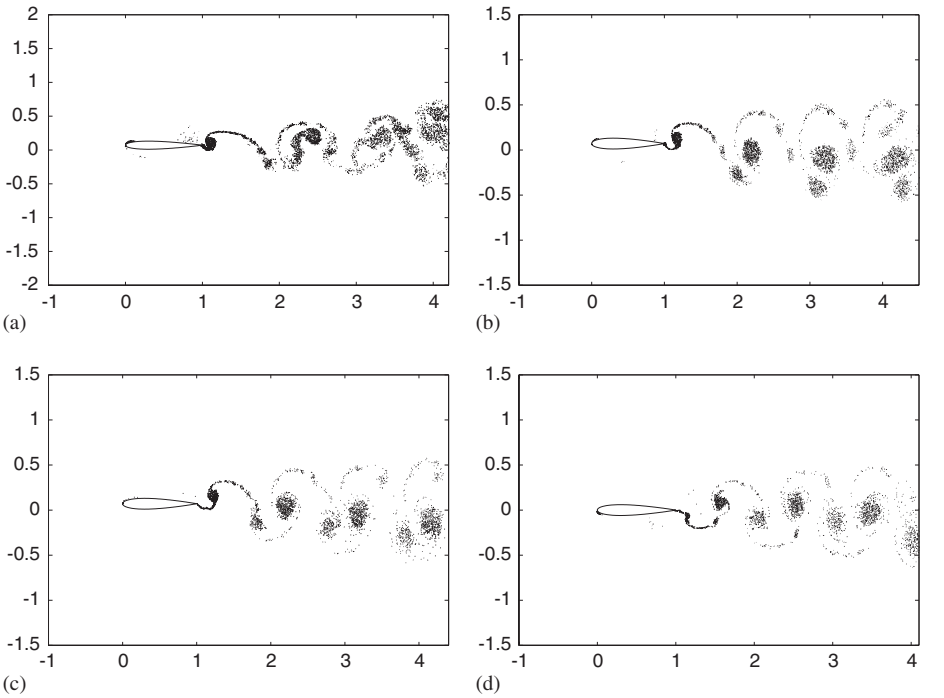


Figure 14. Unsteady wake patterns with different shape functions, $k\bar{h} = 0.5$, $k = 7$: (a) $S = 80\%$; (b) $S = 70\%$; (c) $S = 60\%$; and (d) $S = 50\%$. Instantaneous $h/c = 0.07$ (upstroke) for all asymmetric sinusoidal case, for $S = 50\%$, airfoil is at the mean position downwards.

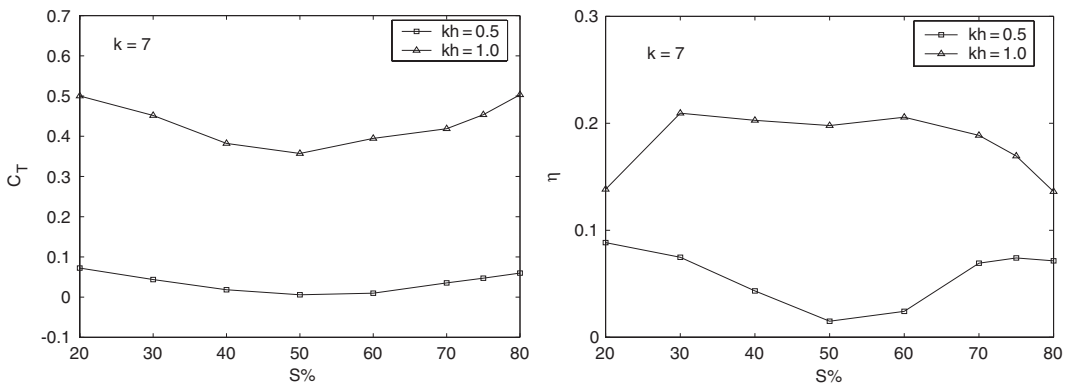


Figure 15. Average thrust coefficient and propulsive efficiency for asymmetric sinusoid heaving.

At the points where the constant heave rate changes sign discontinuously, the drag coefficient also changes abruptly. The time history of the drag coefficient has been shown in Figure 20(a) with the random noise present in it. The random noise is present due to the

 

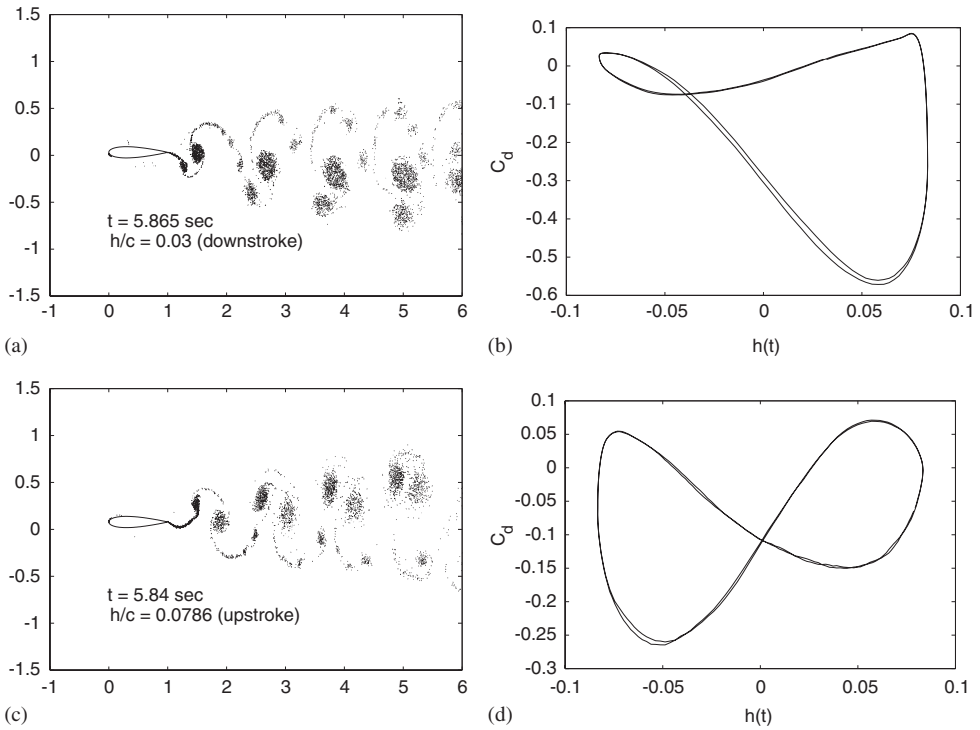


Figure 16. $k\bar{h} = 0.5$; $k = 6$. Opposite initial condition: (a) and (b) $S = 30\%$; and (c) and (d) $S = 60\%$.

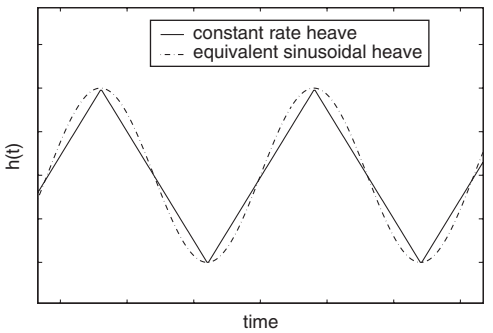


Figure 17. A typical qualitative plot showing constant rate heaving motion and its equivalent sinusoidal heaving motion.

random walk model for the diffusion process. However, a moving average in time is done to eliminate the noise, [19]. However, as Figure 20(b) shows, this averaging process cannot capture the exact location of the sharp discontinuity in the response. It smoothens out the response to some extent. The drag coefficient versus heave displacement plot for all the different cases of constant rate case is shown after the time averaging. It should be noted here

 

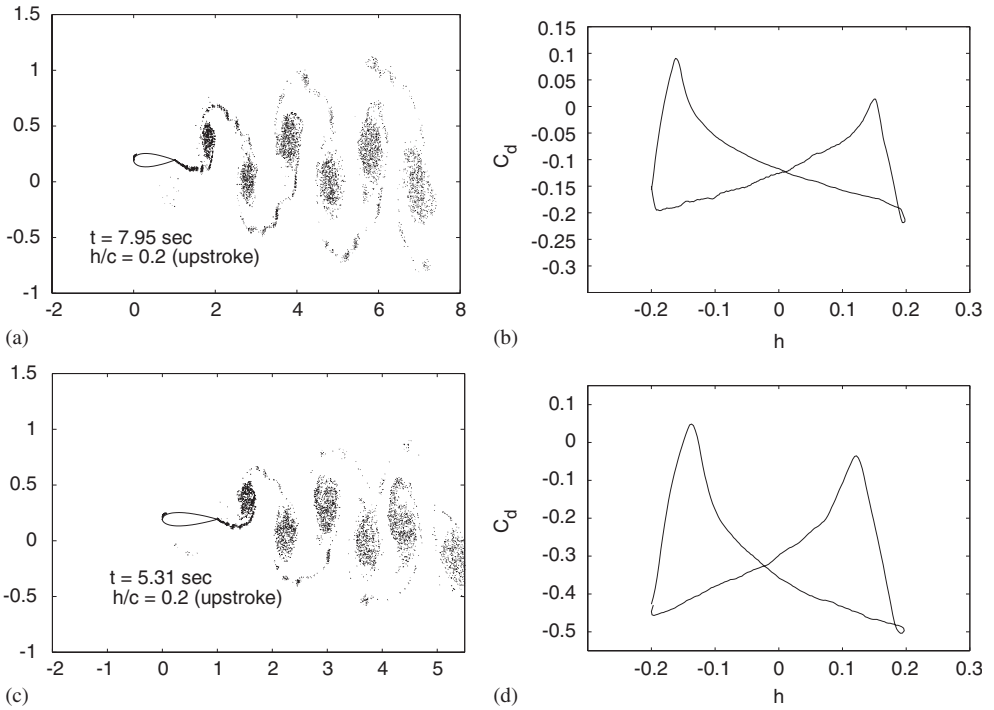


Figure 18. Constant rate heave oscillation. Wake pattern and drag coefficient history, $\bar{h} = 0.2$: (a) and (b) $v_o/\mathbf{V}_\infty = 0.4$; and (c) and (d) $v_o/\mathbf{V}_\infty = 0.6$.

that for continuous response, such averaging does not affect the system response characteristics qualitatively.

The average drag coefficient and the propulsive efficiency for the constant rate cases as well as their corresponding sinusoidal cases have been plotted in Figure 21. The thrust coefficient versus non-dimensional rate plot follows the same trend as well as almost have the same values as in the sinusoidal case. The propulsive efficiency though is lower, in general, for the constant rate case.

### *4.4. Sinusoidal pulses*

Sinusoidal pulse trains could serve as models for certain types of animal locomotion. We therefore studied sinusoidal heaving motion with a quiescent gap, repeated many times as shown in Figure 22(a). $T$ is the time period of the sinusoidal part and the gap period for which the heaving oscillation is zero is given by a fraction ($fa$) of the time period $T$. We have considered two different cases with $fa = 2$ and 4. The wake pattern for such types of motion is quite different than all the earlier cases presented here. Large deflection of the wake is obtained during the quiescent gap period of the motion as shown in Figure 22(b). Note that the large downward deflection of the wake is associated with large impulse imparted to the wake when the airfoil is stationary for some time interval $T/fa$. This is to be contrasted with the impulses imparted to the fluid in the constant-rate heave case shown in Figures 18

 

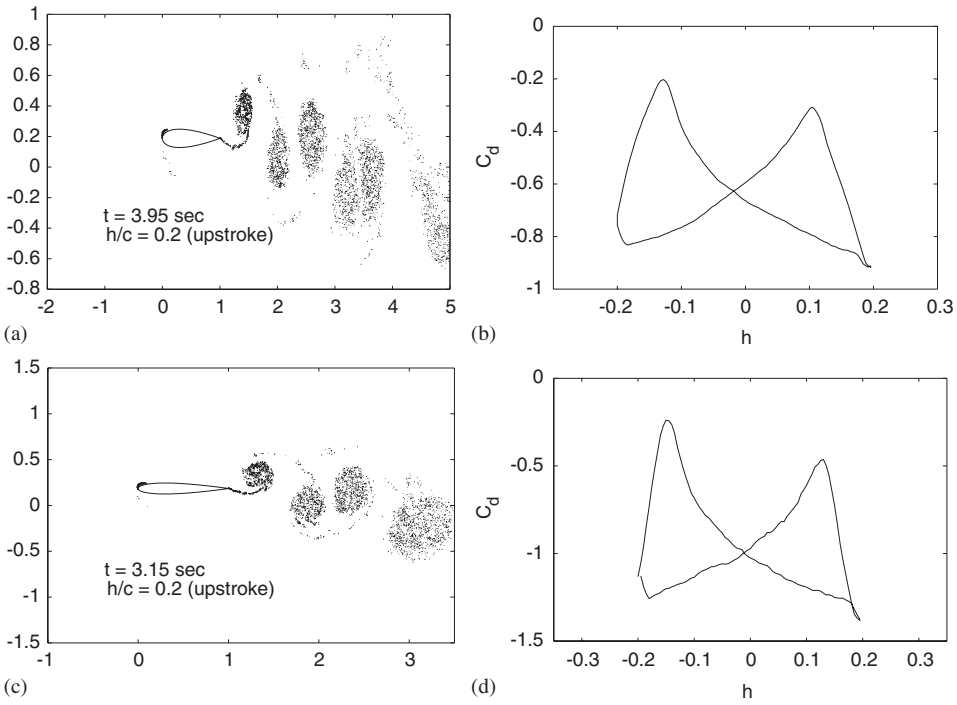


Figure 19. Constant rate heave motion. Wake pattern and drag coefficient history, $\bar{h} = 0.2$: (a) and (b) $v_o/\mathbf{V}_\infty = 0.8$; and (c) and (d) $v_o/\mathbf{V}_\infty = 1.0$.

and 19. There, despite the presence of a discontinuity in the rate at the end of the upstroke and downstroke, it does not result in large wake displacement. The heave rate changes sign there and the wake is pulled in an opposite direction to what it was before. In the present case, the heave rate changes from a positive or negative value to zero. What one sees as a wake displacement is the drift of the trailing edge vortex.

The drag coefficients have been plotted for both the cases in Figure 23. Note the large change in the drag coefficient during the time interval the airfoil is stationary.

Table I compares the average load coefficients and the propulsive efficiencies for both the cases with the corresponding sinusoidal case. Expectedly, the thrust force for the sinusoidal case without gap is maximum. However, the propulsive efficiency is also higher for the sinusoidal case.

## 5. CONCLUSION

The present work addresses the problem of thrust generated by an airfoil oscillating in a not purely sinusoidal motion. We have considered three classes of motions. One is the asymmetric sinusoid which is a sinusoid excepting that the upstroke is faster/slower than the downstroke. The asymmetry parameter $S$ defines the fraction of the time-period it takes to complete the

 

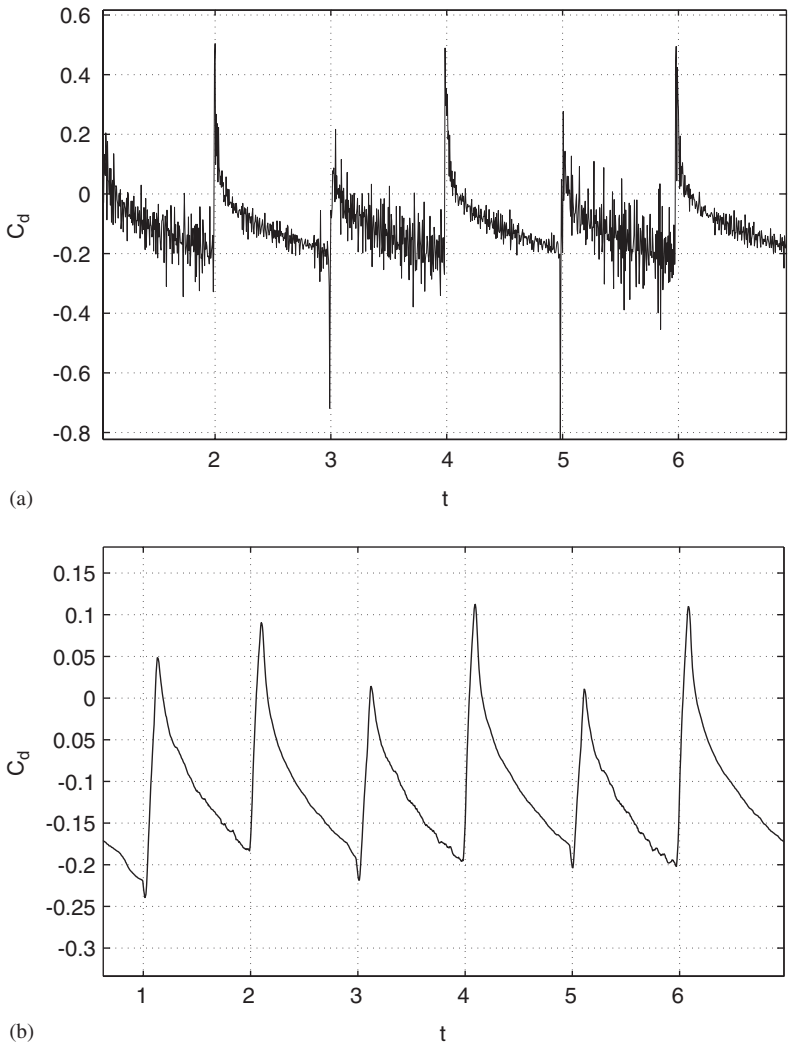


Figure 20. Constant rate heave motion, $\bar{h} = 0.2$: (a) drag time history for rate = 0.4; and (b) drag time history after time averaging for rate = 0.4.

downstroke. The second type of motion considered is the constant heave rate in the upstroke and downstroke. This results in a triangular waveform. The third and final type of motion studied is the sinusoidal pulse train. These type of motions consists of a sinusoidal oscillation followed by a time-interval in which the airfoil is stationary. There are significant differences in the vortex shedding behaviour for all these types of motion. For the asymmetric sinusoidal cases, the wake patterns always look deflected from the mean position. The deflection mode changes as the asymmetry parameter $S$ changes. Another important observation of this asymmetric sinusoidal case is that the vortex pairing pattern changes from cycle to cycle. Also,

 

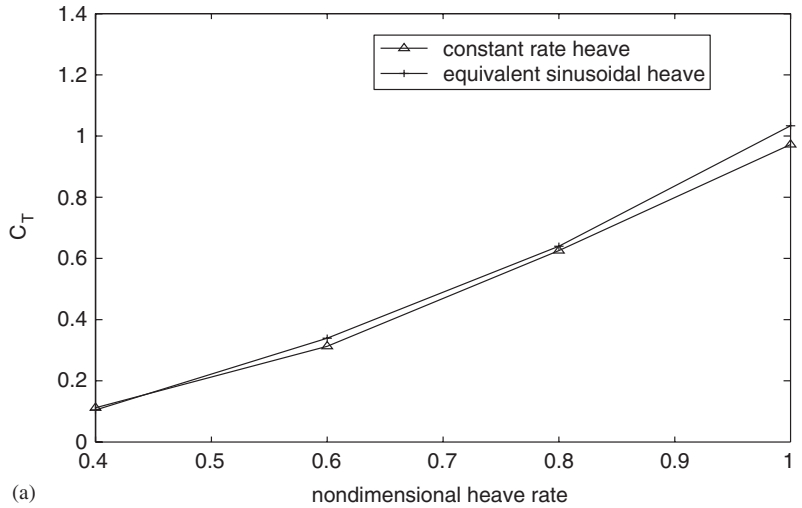


Figure 21. Constant rate heave motion, $\bar{h} = 0.2$: (a) average thrust coefficient; and (b) average propulsive efficiency.

at higher $k\bar{h}$ values, the wake patterns look more diffused. The aerodynamic thrust coefficient and the propulsive efficiency have been compared with their corresponding sinusoidal cases. For all $k\bar{h}$ values, thrust force is minimum for the sinusoidal case. This trend can be explained by looking at the wake patterns. For asymmetric sinusoidal cases, the wake vortex patterns are much more deflected than the perfect sinusoidal cases. This could translate into greater thrust values. However, the propulsive efficiency show different trends at different $k\bar{h}$ values. We have also compared different types of non-sinusoidal motions like constant pitching rates, sinusoid with a gap, etc. with their equivalent sinusoidal motions. However, these cases

 

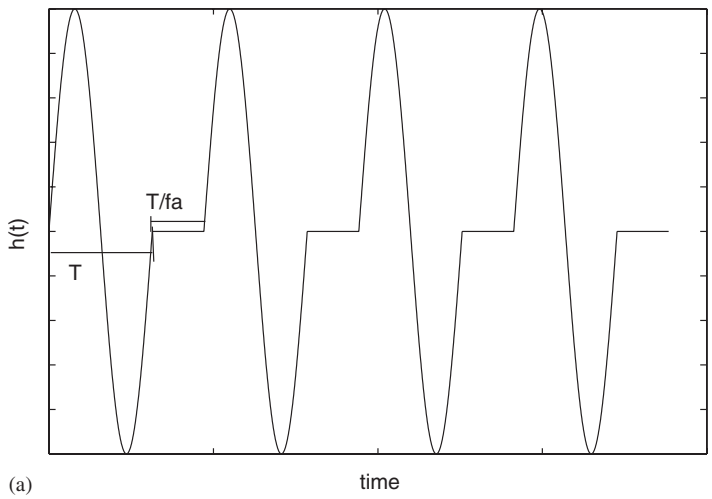


(a)

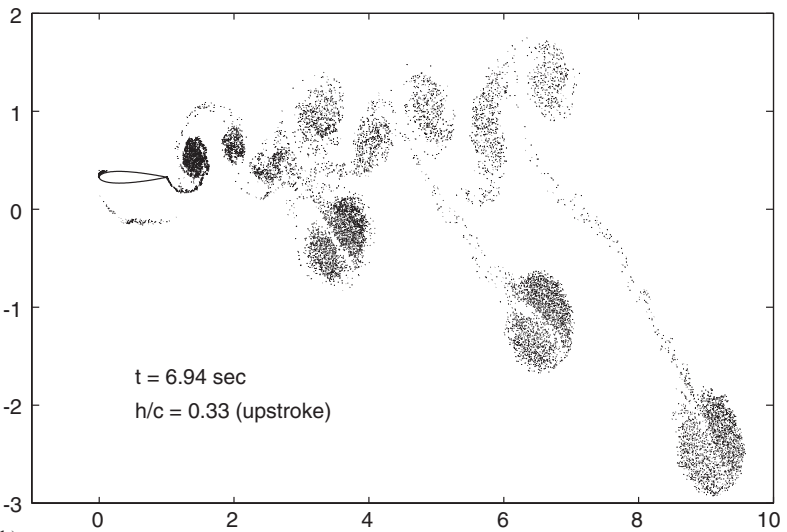


(b)

Figure 22. (a) Schematic plot of a heaving motion described by a sinusoid followed by a gap, heave is zero during $T/fa$, $fa$ is a fraction of the sinusoidal time period; and (b) the wake pattern for such heaving motion; $k\bar{h} = 1.5$; $fa = 4$.

show lesser thrust force as well as smaller propulsive efficiency values than their sinusoidal counterparts.

A random discrete vortex technique has been used for the numerical simulation of the two-dimensional, viscous, unsteady system. A smooth implementation of the method depends on various aspects. One should be careful about choosing the number of vortices generated at each time step. A hugely over estimated vortex point representation can be severely wrong,

 

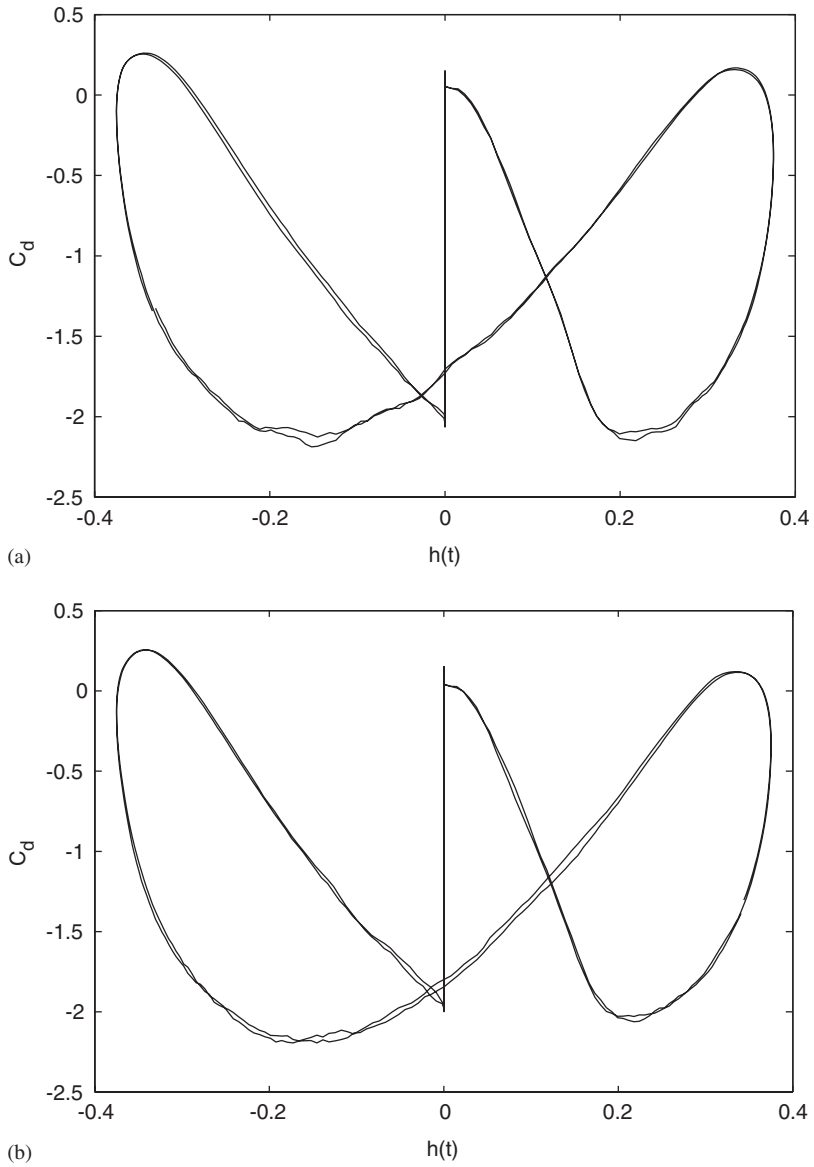


Figure 23. The drag history for sinusoid followed by a gap heaving motion, $k\bar{h} = 1.5$: (a) $fa = 4$; and (b) $fa = 2$.

and too few a number of vortex particles in the flow field may be insufficient to accurately simulate the true physical phenomenon. Further, too small a time step size may restrain the nascent vortices from entering the flow field after crossing the control zone. In that case, if more number of vortices are generated per time step, it may counter this effect to some extent. In other words, more number of panels and sub-panels should be considered. Also,

 

Table I. $C_d$ and $\eta$ for sinusoid with a gap motion.

| | $C_d$ | $\eta$ (s) (%) |
|---|---|---|
| Sinusoid with $k\bar{h} = 1.5$, $k = 4$ | −1.0571 | 23.2 |
| Sinusoid with gap $= T/2$ | −0.6838 | 15.2 |
| Sinusoid with gap $= T/4$ | −0.8257 | 15.6 |

manipulating the thickness of the control zone can be useful. Hence the time step, control zone thickness, and also the number of vortices generated, are somewhat mutually dependent. It needs some trial and error estimation for any simulation to fix the values of these parameters. In the present study, the same set of values for these parameters were used for all simulation cases. We did not change them as good convergence was obtained throughout.

This technique requires large number of discrete vortices to be generated in the flow field for better convergence. Depending on the time window of the simulation, the total number of vortices $N$ present in the flow field could be of the order of a few thousands. The computational cost varies as a function of $N^2$, hence the method could computationally become very intensive, and consequently slow down the time marching process for the unsteady problem being simulated. In this regard, it should be mentioned that there are some fast algorithms proposed in the literature that could be useful in bringing down the computational cost. These techniques reduce the computational cost from the order of $N^2$ to $N \log N$ [25], or to $N$ [26], and therefore are faster. Such methods could add some improvement in terms of simulation time especially with slower processors. In the present simulation, the maximum CPU time spent was in the range of 12–16 h on an COMPAQ AlphaServer ES 40 (non-parallel environment), and we did not employ any fast algorithm.

## REFERENCES

1. Triantafyllou MS, Triantafyllou GS, Yue DKP. Hydrodynamics of fish-like swimming. *Annual Review of Fluid Mechanics* 2000; **32**:33–53.
2. Garrick IE. Propulsion of a flapping and oscillating airfoil. *TR 567*, NACA, 1936.
3. Lighthill MJ. Aquatic animal propulsion of high hydromechanical efficiency. *Journal of Fluid Mechanics* 1970; **44**(part 2):265–301.
4. Jones KD, Dohring CM, Platzer MF. Experimental and computational investigation of the Knoller–Betz effect. *AIAA Journal* 1998; **36**(7):1240–1246.
5. Tuncer IH, Platzer MF. Computational study of flapping airfoil aerodynamics. *Journal of Aircraft* 2000; **37**(3):514–520.
6. Triantafyllou GS, Triantafyllou MS, Grosenbaugh MA. Optimal thrust development in oscillating foils with application to fish propulsion. *Journal of Fluids and Structures* 1993; **7**:205–224.
7. Lai JCS, Platzer MF. Jet characteristics of a plunging airfoil. *AIAA Journal* 1999; **37**(12):1529–1537.
8. Lewin JC, Haj-Hariri H. Modelling thrust generation of a two-dimensional heaving airfoil in a viscous flow. *Journal of Fluid Mechanics* 2003; **492**:339–362.
9. Wang ZJ. Vortex shedding and frequency selection in flapping flight. *Journal of Fluid Mechanics* 2000; **410**:323–341.
10. Isogai K, Shinmoto Y, Watanbe Y. Effects of dynamic stall on propulsive efficiency and thrust of flapping airfoil. *AIAA Journal* 1999; **37**(10):1145–1151.
11. Anderson JM, Streitlien K, Barrett DS, Triantafyllou MS. Oscillating foils of high propulsive efficiency. *Journal of Fluid Mechanics* 1998; **360**:41–72.
12. Read DA, Hover FS, Triantafyllou MS. Forces on oscillating foils for propulsion and maneuvering. *Journal of Fluids and Structures* 2003; **17**:163–183.
13. Hover FS, Haugsdal O, Triantafyllou MS. Effect of angle of attack profiles in flapping foil propulsion. *Journal of Fluids and Structures* 2004; **19**:37–47.

 

14. Koochesfahani MM. Vortical patterns in the wake of an oscillating airfoil. *AIAA Journal* 1989; **27**(9): 1200–1205.
15. Batchelor GK. *An Introduction to Fluid Dynamics*. Cambridge University Press: New Delhi, 1967.
16. Tang T, Ingham DB. On steady flow past a rotating circular cylinder at Reynolds numbers 60 and 100. *Computers and Fluids* 1991; **19**(2):217–230.
17. Wu JC, Thompson JF. Numerical solutions of time-dependent incompressible Navier–Stokes equations using an integro-differential formulation. *Computers and Fluids* 1973; **1**:197–215.
18. Lin H, Vezza M, Galbraith RAMcD. Discrete vortex method for simulating unsteady flow around pitching aerofoils. *AIAA Journal* 1997; **35**(3):494–499.
19. Chorin AJ. Numerical study of slightly viscous flow. *Journal of Fluid Mechanics* 1973; **57**(4):785–796.
20. Sarpkaya T. Computational methods with vortices—the 1988 Freeman scholar lecture. *Journal of Fluids Engineering* 1989; **111**:5–52.
21. Koumoutsakos P, Leonard A, Pepin F. Boundary conditions for viscous vortex methods. *Journal of Computational Physics* 1994; **113**:52–61.
22. Schmall RA, Kinney RB. Numerical study of unsteady viscous flow past a lifting plate. *AIAA Journal* 1974; **12**:1566–1573.
23. Lighthill MJ. Introduction. Boundary layer theory. In *Laminar Boundary Layers*, Rosenhead J (ed.). Oxford University Press: New York, 1963; 54–61.
24. Katz J, Plotkin A. *Low Speed Aerodynamics*. Cambridge University Press: Cambridge, 2001.
25. Greengard L, Rokhlin V. A fast algorithm for particle simulations. *Journal of Computational Physics* 1987; **73**:325–348.
26. van Dommelen L, Rundsteiner EA. Fast, adaptive summation of point forces in the two-dimensional Poisson equation. *Journal of Computational Physics* 1989; **83**:126–147.
27. Leonard A. Direct numerical simulation of turbulent flows. *Computers and Fluids* 1973; **1**:197–215.

 